



1           **A merged continental planetary boundary layer height**  
2           **dataset based on high-resolution radiosonde measurements,**  
3                           **ERA5 reanalysis, and GLDAS**

4  
5           Jianping Guo<sup>a</sup>, Jian Zhang<sup>b\*</sup>, Tianmeng Chen<sup>a</sup>, Kaixu Bai<sup>c</sup>, Jia Shao<sup>d\*</sup>, Yuping Sun<sup>a</sup>,  
6           Ning Li<sup>a</sup>, Jingyan Wu<sup>a</sup>, Rui Li<sup>c</sup>, Jian Li<sup>a</sup>, Qiyun Guo<sup>f</sup>, Jason B. Cohen<sup>g</sup>, Panmao Zhai<sup>a</sup>,  
7                           Xiaofeng Xu<sup>h</sup>, Fei Hu<sup>i\*</sup>

8  
9  
10           <sup>a</sup>State Key Laboratory of Severe Weather, Chinese Academy of Meteorological  
11                           Sciences, Beijing 100081, China

12           <sup>b</sup>Hubei Subsurface Multi-scale Imaging Key Laboratory, Institute of Geophysics and  
13                           Geomatics, China University of Geosciences, Wuhan 430074, China

14           <sup>c</sup>Key Laboratory of Geographic Information Science (Ministry of Education), School of  
15                           Geographic Sciences, East China Normal University, Shanghai 200241, China

16           <sup>d</sup>College of Informatics, Huazhong Agricultural University, Wuhan 430070, China

17           <sup>e</sup>Ministry of Education Key Laboratory for Earth System Modeling, Department of  
18                           Earth System Science, Tsinghua University, Beijing 100084, China

19           <sup>f</sup>Meteorological Observation Center, China Meteorological Administration, Beijing  
20                           100081, China

21           <sup>g</sup>School of Environment and Spatial Informatics, China University of Mining and  
22                           Technology, Xuzhou, China

23           <sup>h</sup>China Meteorological Administration, Beijing 100081, China

24           <sup>i</sup>State Key Laboratory of Atmospheric Boundary Layer Physics and  
25                           Atmospheric Chemistry, Institute of Atmospheric Physics, Beijing 100029, China

26

27

28           Correspondence to:

29           Dr. Jian Zhang (Email: zhangjian@cug.edu.cn), Dr. Jia Shao (Email:  
30           shaojia@mail.hzau.edu.cn and Dr./Prof. Fei Hu (Email: hufei@mail.iap.ac.cn)

31



32 ABSTRACT

33 The planetary boundary layer (PBL) is the lowermost part of the troposphere that  
34 governs the exchange of momentum, mass and heat between surface and atmosphere.  
35 To date the radiosonde measurements have been extensively used to estimate PBLH;  
36 suffering from low spatial coverage and temporal resolution, the radiosonde data is  
37 incapable of providing the diurnal description of PBLH across the globe. To fill this  
38 data gap, this paper aims to produce a temporally continuous PBLH dataset during the  
39 course of a day over the global land by applying the machine learning algorithms to  
40 integrate high-resolution radiosonde measurements, ERA5 reanalysis, and GLDAS  
41 product. This dataset covers the period from 2011 to 2021 with a temporal resolution  
42 of 3-hour and a horizontal resolution of  $0.25^{\circ} \times 0.25^{\circ}$ . The radiosonde dataset contained  
43 around 180 million profiles over 370 stations across the globe. The machine learning  
44 model was established by taking 18 parameters derived from ERA5 reanalysis and  
45 GLDAS as input variables while the PBLH biases between radiosonde observations  
46 and ERA5 reanalysis were used as the learning targets. The input variables were  
47 presumably representative regarding the land properties, near-surface meteorological  
48 conditions, terrain elevations, lower tropospheric stabilities, and solar cycles. Once a  
49 state-of-the-art model had been trained, the model was then used to predict the PBLH  
50 bias at other grids across the globe with parameters acquired or derived from ERA5 and  
51 GLDAS. Eventually, the merged PBLH can be taken as the sum of the predicted PBLH  
52 bias and the PBLH retrieved from ERA5 reanalysis. Overall, this merged high-  
53 resolution PBLH dataset was globally consistent with the PBLH retrieved from  
54 radiosonde observations both in magnitude and spatiotemporal variation, with a mean  
55 bias of as low as  $-0.9$  m. The dataset and related codes are publicly available at  
56 <https://doi.org/10.5281/zenodo.6498004> (Guo et al., 2022), which are of significance  
57 for a multitude of scientific research and applications, including air quality, convection  
58 initiation, climate and climate change, just to name a few.

59

60



## 61 **1. Introduction**

62 Planetary boundary layer (PBL), the lowermost part of the troposphere where the  
63 turbulence and convection mainly occur, is of significance in modulating the exchange  
64 of momentum, heat, moisture, and mass between the surface and the free atmosphere  
65 over a range of scales (Stull 1988; Cooper and Eichinger, 1994; Edson et al., 2013).  
66 The turbulence in the PBL is largely generated mechanically, which is owing to both  
67 wind shear and friction, and is generated convectively, which is owing to buoyancy and  
68 surface heating (Degrazia et al., 2020). Within the PBL, vertical turbulent mixing of air  
69 masses is rapid and constant, on the order of 30 minutes or less (Wallace and Hobbs,  
70 2006). Therefore, the reliable parameterization of the PBL is crucial for the accurate  
71 representations of vertical diffusion, cloud formation/development, and pollutant  
72 deposition in numerical weather prediction (NWP), climate, air quality and coupled  
73 atmosphere–hydrosphere–biosphere models (Seibert, 2000; Hu et al., 2010; Baklanov  
74 et al., 2011). It has been well recognized that the variation of PBL height (PBLH)  
75 significantly impacts the near-surface air quality (Petäjä et al., 2016; Wang and Wang,  
76 2016; Lou et al., 2019; Li et al., 2021) and climate system as well (Esau and  
77 Zilitinkevich, 2010; Davy and Esau, 2016).

78 The development of PBL is subject to the changes of the energy balance near the  
79 ground surface, largely through the linkages between soil moisture and sensible heat  
80 flux, latent heat flux and net radiation (Dirmeyer et al., 2014; Xu et al., 2021). In  
81 particular, the sensible heat flux is closely associated with the variation in  
82 evapotranspiration, land type, and cloud cover. Also, the daytime convective PBL is  
83 modulated by cloud radiative effects, particularly in the early afternoon (Guo et al.,  
84 2016; Zhang et al., 2018; Davis et al., 2020). Furthermore, the aerosol radiative effect  
85 (due to both aerosol scattering and absorption) indirectly affects the evolution of PBL  
86 by changing the atmospheric heating rate and the solar radiation reaching the surface  
87 (Wang et al., 2013; Li et al., 2017; Yang et al., 2016). Besides, the entrainment of air  
88 from above the PBL can also significantly drive the evolution of PBL (Hu et al., 2010).



89 To date, a variety of methods have been applied on vertical profiles of aerosol  
90 properties, water vapor, temperature, refractivity, and wind to estimate PBLH (e.g.,  
91 Holzworth 1964; Seibert 2000; Lammert and Bösenberg 2006; McGrath-Spangler and  
92 Denning 2012; Chan and Wood 2013; Su et al., 2018; Liu et al., 2019; Ding et al., 2021).  
93 The estimate varies considerably with data sources, algorithms, and data vertical  
94 resolutions (Seibert et al., 2000; Seidel et al., 2010). For instance, PBLH determined by  
95 the minimum vertical gradient relative humidity is about 1 km larger than that from the  
96 parcel method, even though the latter algorithm is generally thought to be one of the  
97 most reliable methods for the estimation of the convective boundary layer (CBL) height  
98 (Hennemuth and Lammert, 2006; Seidel et al., 2010). In addition, different data sources,  
99 such as ceilometer Lidar, COSMIC GPS RO satellite, radiosonde, and ERA5 reanalysis  
100 dataset can reach quite different estimates of PBLH (Saha et al., 2022). Recently, as  
101 suggested by Teixeira et al. (2021), the PBLH should be ideally estimated using direct  
102 observations of vertical profiles of turbulent quantities, which is due in large part to the  
103 turbulent nature of PBL. But only a few places have such observations. A wide range  
104 of complex physical and chemical processes involved in the PBL further make PBLH  
105 estimates quite elusive and tricky (Seidel et al., 2010; Teixeira et al., 2021).

106 Among the instruments, radiosonde is the most accepted instrument for deriving  
107 the CBL and stable boundary layer (SBL), due to the ability to characterize the  
108 thermodynamic and dynamic states of the boundary layer (Seidel et al., 2010; de Arruda  
109 Moreira et al., 2018, Guo et al., 2019). In addition, the bulk Richardson number method  
110 has been proved to be the most suitable PBLH algorithm for application to a large  
111 radiosonde dataset (Seidel et al., 2012). The dataset with a full vertical resolution (5–8  
112 m) has previously been used to study PBLHs over China and near-globe (Guo et al.,  
113 2016; 2021). The limitation of this dataset is its poor coverage over the ocean and some  
114 continental areas without radiosonde observations, such as Africa and Central Asia.

115 By contrast, reanalysis datasets, such as the fifth generation ECMWF (European  
116 Centre for Medium-Range Weather Forecasts) atmospheric reanalysis (ERA5) and the  
117 Modern-Era Retrospective-analysis for Research and Applications version 2 product



118 (MERRA-2), have a unique advantage in spatial-temporal coverage. Our recent study  
119 suggests that ERA5 is the most promising reanalysis data source in terms of  
120 characterizing the evolution of PBLH, with an underestimation of daytime PBLH at  
121 around 130 m, when compared to high-resolution radiosonde (Guo et al., 2021).  
122 Nevertheless, the underestimation of PBLH in ERA5 reanalysis can be as high as 500  
123 m in the afternoon when the PBL is fully developed. This underestimation could be  
124 attributed to, but not limited to, the gradient of terrain elevation and the lower  
125 tropospheric stability.

126 Rather, by exploiting both the advantages of in situ atmospheric measurements  
127 from radiosonde and the high-resolution model products from ERA-5 reanalysis, it is  
128 quite desirable to generate a new PBLH dataset by seamlessly blending these versatile  
129 products. The biases between PBLH retrieved from the ERA-5 and radiosonde could  
130 be optimized via a machine learning model. To this end, the present analyses used the  
131 radiosonde dataset that contained around 180 million profiles over 370 stations across  
132 the world, as well as ERA5 reanalysis, and GLDAS data. A long-term merged PBLH  
133 dataset covering the period 2011 to 2021 were generated, which could have crucial  
134 implications for the development and evaluation of weather and climate, environmental  
135 meteorology, and boundary layer parameterization. The rest of the paper is organized  
136 as follows. Section 2 describes the fundamental data sets and the PBLH methodology  
137 we use in this study, Sections 3 and 4 report on the machine learning algorithm used to  
138 generate the merged PBLH dataset, also revealed are the data quality, and Section 5  
139 represents the climatological merged continental PBLH, and Section 6 ends with a brief  
140 summary and conclusion.

## 141 **2. Data sources and conventional PBLH determination method**

### 142 2.1 High-resolution radiosonde measurements

143 As described in Guo et al. (2021) and Zhang et al. (2022), a high-resolution  
144 radiosonde dataset gained from several organizations was adopted, spanning the years



145 from 2011 to 2021. The organizations include the China Meteorological Administration  
146 (CMA), the National Oceanic and Atmospheric Administration (NOAA), the Global  
147 Climate Observing System (GCOS) Reference Upper-Air Network (GRUAN), the  
148 Centre for Environmental Data Analysis of the United Kingdom (CEDA), University  
149 of Wyoming, and German Deutscher Wetterdienst. The detailed information on the  
150 provided data is listed in Table 1. In total, 185 million radiosonde profiles were  
151 collected to determine PBLH, 95% of which were released at regular synoptic times of  
152 0000 UTC and 1200 UTC, and the rest of them were irregularly launched at other times.  
153 Note that those soundings with the lowest burst height lower than 10 km above ground  
154 level (a.g.l) were eliminated. In addition, all the profiles were evenly interpreted to 10  
155 m resolution in the vertical direction by cubic spline interpolation.

156 The spatial distribution of sample numbers over each radiosonde station at four  
157 different synoptic times (0000 UTC, 0600 UTC, 1200 UTC, 1800 UTC) is presented in  
158 Figure 1. It is noticeable that the radiosonde stations over Europe, the U.S., China, and  
159 Australia have a spatially even coverage. Furthermore, the observation over China and  
160 the U.S. has a fair temporal continuity at 0000 UTC and 1200 UTC, with a total sample  
161 number as large as 3000 for each station. In comparison, the stations are poorly  
162 distributed over regions or countries such as southern America, the Pacific islands,  
163 Russia, the Middle East, India, and Africa.

## 164 2.2 ERA5 and GLDAS

165 ERA5 is the latest version of ECMWF reanalysis, benefiting from a decade of  
166 developments in model physics, core dynamics, and data assimilation (Hersbach et al.,  
167 2020). The PBLH product is resolved by the ERA5 reanalysis on a  $1440 \times 721$   
168 longitude/latitude grid, with a spatial resolution of  $0.25^\circ \times 0.25^\circ$  and a temporal  
169 resolution of 1 hour, which is realistically simulated by the bulk Richardson number  
170 method. In addition, the parameters, such as the lower tropospheric stability (LTS), the  
171 standard deviation of digital elevation model (SDDDEM), 10-m surface wind speed, 2-  
172 m air temperature, and 2-m pressure, are either computed or directly extracted from



173 ERA5 reanalysis. LTS is defined as the difference in potential temperature between the  
174 700 hPa level and 1000 hPa. As a result, a total of six parameters were obtained based  
175 on ERA5 reanalysis.

176 The land property parameters were taken from NASA Global Land Data  
177 Assimilation System (GLDAS), which include downward short-wave radiation  
178 (DSWR), downward long-wave radiation (DLWR), surface heat net flux (SHF), surface  
179 latent heat net flux (LHF), evapotranspiration, transpiration, soil moistures in 0–10 cm,  
180 10–40 cm, 40–100 cm, and 100–200 cm, and total precipitation rate. Totally, 11  
181 parameters were extracted from the GLDAS product. GLDAS has a temporal resolution  
182 of 3 hours and the same spatial resolution as that of ERA5 reanalysis. However,  
183 GLDAS has no data over Antarctica. The start latitude and longitude of GLDAS are  
184 0.125° lag of ERA5 and therefore, the latitude and longitude of GLDAS will be minus  
185 0.125, to match with ERA5 reanalysis.

### 186 2.3 PBLH determination by using bulk Richardson number method

187 The bulk Richardson number (Ri) is widely used for the climatological study of  
188 PBLH from radiosonde measurements thanks to its applicability and reliability for all  
189 atmospheric conditions (Anderson 2009; Seidel *et al.*, 2012). Ri, as a good indicator of  
190 turbulence and thermodynamic stability, is calculated as the ratio of turbulence due to  
191 buoyancy to that due to mechanical shear, which is formulated as

$$192 \quad \text{Ri}(z) = \frac{\left(\frac{g}{\theta_{vs}}\right)(\theta_{vz} - \theta_{vs})z_{AG}}{(u_z - u_s)^2 + (v_z - v_s)^2 + (bu_s^2)} \quad (1)$$

193 where  $g$  is the gravitational acceleration,  $z_{AG}$  the AGL,  $\theta_v$  the virtual potential  
194 temperature,  $u_*$  the surface friction velocity,  $u$  and  $v$  the horizontal wind component,  
195 and  $b$  the constant which is usually set to zero since friction velocity is much weaker  
196 compared with the horizontal wind (Seidel *et al.*, 2012). The subscripts of  $z$  and  $s$   
197 denote the parameters at  $z$  height above ground and the ground level, respectively.

198 The critical value of  $\text{Ri}(z)$  can be used to identify a statically stable layer atop the  
199 PBL (Seibert *et al.*, 2000), and it is commonly taken as 0.25. Meanwhile, PBLH  
200 estimates were found varying little by differing the input of critical values ( $\text{Ri} =$



201 0.2; 0.25; 0.3) (Guo et al., 2016). Therefore, the PBLH here is identified as the  
202 interpolated height where  $Ri(z)$  profile crosses the critical value of 0.25. The  
203 determined PBLH was set invalid in these two scenarios: (1) the second level of  $Ri(z)$   
204 in Eq. (1) exceeds 0.25; (2) the estimated PBLH is extremely high (for instance, 10 km),  
205 and it could mistake free-tropospheric features.

### 206 **3. Methodology**

207 As shown in Figure 2, there exist discernable biases between PBLH retrieved from  
208 radiosonde (hereinafter referred to as PBLH-R) and PBLH determined from ERA5  
209 reanalysis (hereinafter referred to as PBLH-E). According to 185 million sounding  
210 measurements (Fig.2a), the PBLH bias (PBLH-R minus PBLH-E) is less dependent on  
211 years, with a mean bias of 95.7 m, indicative of a possible systematic PBLH  
212 underestimation of the ERA5 reanalysis. By contrast, the underestimation is around 137  
213 m during the daytime (Guo et al., 2021), which is systematically larger than that during  
214 all days. However, the bias is found varying with seasons and local solar times (LST).  
215 More precisely, the mean bias varies from 150 m in the March–April–May (MAM) to  
216 64 m in the September–October–November (SON), and from 309 m at 1700 LST to 1.8  
217 m at 0000 LST. Moreover, the standard deviation of bias greatly changes from 64 m at  
218 0100 LST to 807 m at 1700 LST. The large uncertainty raised by PBLH-E during the  
219 daytime motivated this study to establish a new PBLH dataset that would be more  
220 consistent with observations.

221 The bias could be statistically attributed to the variables such as SDDEM and LTS  
222 (Guo et al., 2021). However, the potential correlation with other variables, including  
223 DLWR, DSWR, SHF, LHF, evapotranspiration, transpiration, total precipitation rate  
224 (TPR), soil moistures (SMs), as well as wind speed, pressure, and air temperature at the  
225 near surface, has not been systematically discussed yet. As shown in Figure 3, the bias  
226 is positively correlated with SHF, transpiration, LTS, and 2-m near-surface temperature,  
227 with a correlation coefficient ranging from 0.39 to 0.9 based on 10 evenly split bins.  
228 However, these parameters could be independent. For instance, evapotranspiration is



229 determined by surface features which include plant physiology, land cover, and soil  
230 moisture, and it is the most important non-radiative process transmitting latent heat  
231 from the surface to the atmosphere (Cuxart and Boone, 2020). In addition, soil moisture  
232 probably contributes to decreases in the surface sensible flux locally (Basha and  
233 Ratnam, 2009). The correlation coefficients and their confidence levels between PBLH  
234 bias and these variables are presented in Table 2, according to all samples.

235 Based on these findings, it is found that the PBLH bias is highly associated with  
236 the variations in land properties, near-surface meteorological conditions, terrain  
237 elevations, lower tropospheric stabilities, and solar cycles. Consequently, it is possible  
238 to predict the PBLH bias based on these potential influential variables. Once the  
239 spatially resolved bias is available, a bias corrected PBLH dataset, namely, a merged  
240 PBLH product (denoted as PBLH-M hereafter), can be acquired by perturbing PBLH-  
241 E with the addition of predicted bias. This process can be formulated as

$$242 \quad PBLH - M = PBLH_{bias} + PBLH - E \quad (2)$$

243 where  $PBLH_{bias}$  denotes the PBLH bias to be predicted. Under this philosophy, here  
244 we established a data-driven  $PBLH_{bias}$  prediction model, with abovementioned factors  
245 used as the potential input variables while the PBLH bias over radiosonde sites as the  
246 learning target. Considering the possible dependence on magnitude of PBLH-E and its  
247 corresponding LST, these two factors were also used as covariates in predicting PBLH  
248 bias.

249 After testing with several machine learning models, such as the ridge regression,  
250 the decision tree regressor, the support vector regressor, the multilayer perceptron  
251 regression, and random forest (RF), we find the latter method gives the most proper and  
252 robust prediction. Therefore, a RF regressor is established to give a prediction of  
253  $PBLH_{bias}$ , and it can be described as

$$254 \quad PBLH_{bias} = RF(DSWR, DLWR, LHF, SHF, EP, TP, SM10, SM40, SM100, \\ 255 \quad \quad \quad SM200, TPR, PBLHE, LTS, SDDEM, NSP, NST, NSWS, LST) \quad (3)$$

256 where the abbreviation RF represents the random forest regressor, and the other  
257 acronyms and abbreviations are listed in Tab.2. In the RF model, the hyper-parameters



258 of the maximum depth of the tree and the random state of the bootstrapping of the  
259 samples are compiled to 20 and 5 in this analysis, respectively. The dataset that contains  
260 the input array and the learning target is randomly divided into two parts, with 70% for  
261 training and 30% for validation. The following statistical metrics, including the mean  
262 squared error (MSE), root mean square error (RMSE), arithmetic mean, and arithmetic  
263 mean of the absolute difference, are applied to evaluate the performance of the  
264 prediction model.

#### 265 **4 Validation**

266 Table 3a presents the prediction accuracy on the training and testing sets. Overall,  
267 the RMSE and arithmetic mean on the training subset are 243 and  $-0.2$ , respectively.  
268 In comparison, these two metrics are 370 and  $-2.8$  on the testing subset, implying the  
269 presence of slight overfitting. To demonstrate the merit of PBLH-M, we further  
270 compare the PBLH bias before and after merging. As illustrated in Fig.4a, the mean  
271 bias between PBLH-R and PBLH-M is  $-0.9$  m, which is smaller than the bias between  
272 PBLH-R and PBLH-E. In addition, the mean of absolute bias decreases from 260 m  
273 (PBLH-R minus PBLH-E) to 168 m (PBLH-R minus PBLH-M), and the standard  
274 derivation declines from 472 m to 241 m, as listed in Tab. 3b. Moreover, the correlation  
275 coefficient between PBLH-R and PBLH-E is 0.59, and it increases to 0.92 between  
276 PBLH-R and PBLH-M. More importantly, the bias between PBLH-R and PBLH-M  
277 during the daytime is dramatically decreased to 20 m, compared to the bias between  
278 PBLH-R and PBLH-E (300 m). These metrics clearly demonstrate a better accuracy of  
279 PBLH-M than PBLH-E, indicative of the merit of correcting modeling biases in PBLH-  
280 E.

281 Furthermore, the overview of PBLH bias (PBLH-R minus PBLH-M) in terms of  
282 spatial variation, and the seasonal variations over the four regions of interest are  
283 presented in Figure 5. As compared to the finding in Guo et al. (2021), the bias  
284 dramatically decreases to dozens of meters for all the stations (Fig. 5d), many of which



285 slightly overestimate PBLH. More specifically, the PBLH over East Asia is  
286 overestimated by around 6 m (Fig.5f), whereas it is underestimated by around 1 m over  
287 Northern America (Fig. 5a). Based on the bias with near-global coverage, we could  
288 infer that the merged model gives a more realistic PBLH estimate.

289 Intensive radiosonde observation is conducted across China in boreal summer  
290 season at 0600 UTC (1400 Beijing Time) when the PBL is fully developed (Zhang et  
291 al., 2018). In addition to the overall near-global spatial distribution, a deeper  
292 investigation of PBLH-M across China at 0600 UTC is presented in Figure 6. The  
293 spatial distribution of PBLH-M exhibits a pronounced “Northwest High Southeast Low”  
294 spatial pattern (Figure 6a), which agrees with Zhang et al. (2018). The correlation  
295 coefficient between PBLH-M and PBLH-R is as high as 0.99, indicating their extreme  
296 consistencies in terms of spatial variations. The annual variations in PBLH-M, PBLH-  
297 R, and PBLH-E follow a similar trend, achieving a maximum in 2013 and a minimum  
298 in 2019 (Fig.6b). The variations in PBLH-M and PBLH-R are rather close to each other.  
299 However, PBLH-E creates a different temporal variation, and it is systematically  
300 underestimated, compared to PBLH-R.

301 As a good case in point for the comparison of fine structures, we show the diurnal  
302 variation of PBLH-M and PBLH-R at 0600 UTC over three stations in Figure 7. Three  
303 sites, including one in northwestern China where the highest PBLH is usually obtained,  
304 one in northern China where the most intensive observations can be found, and one in  
305 southern China where the lowest PBLH can be detected. The diurnal variations of  
306 PBLH-M and PBLH-R are strongly correlated with the lowest correlation of 0.88  
307 (Fig.7d). From Figs. 5-7, we can observe that the spatial-temporal variations of PBLH-  
308 M and PBLH-R are in good agreement.

## 309 **5 Merged continental planetary boundary layer height**

310 The climatological mean of PBLH-M in four seasons at 0000, 0600, 1200, and 1800  
311 UTCs during the years from 2011 to 2021 is illustrated in Figure 8, and the PBLH-R at



312 the same UTC and in the same season are overlaid as filled circles. At all UTCs and in  
313 all seasons the PBLH-M is considerably high during the daytime and reaches a  
314 maximum of around 2 km, especially in the afternoon, as compared to the nighttime. In  
315 addition, PBLH-M experiences a noticeable seasonal variation. For instance, over  
316 Australia, the PBLH-E in SON and December–January–February (DJF) seasons is  
317 about 400 m larger than those of the other two seasons (Fig.8a–d), and vice versa in the  
318 Northern Hemisphere. Moreover, we can observe that PBLH-M has a clear latitude-  
319 and elevation-dependent. It decreases from approximately 2 km at low and middle  
320 latitudes to around 0.8 km at high latitudes during the daytime. At similar latitudes, the  
321 PBLH-M over terrain with a high elevation could be substantially larger than that with  
322 a low elevation. For example, in MAM season and at 1800 UTC the PBLH-E over the  
323 Andes Mountain is about 0.6 km higher than that over the surrounding flat region (Fig.  
324 8m). In a short conclusion, the spatial-temporal variability of the PBLH-M is inevitably  
325 associated with local times, seasons, latitudes, terrain elevations, and hemispheres.

326 In general, PBLH-M is remarkably consistent with PBLH-R in terms of seasonal  
327 variation and diurnal cycle, especially at 0000 UTC and 1200 UTC when the radiosonde  
328 measurement is comparatively sufficient. These findings suggest that the PBLH-M  
329 could adequately resolve the climatological variation of PBLH.

330 The difference in PBLH-M and PBLH-E during the years 2011–2021 at four  
331 typical times is further illustrated in Figure 9. Compared to PBLH-E, the PBLH-M is  
332 overall overestimated, with a mean overestimation of approximately 90 m. The  
333 overestimation appears very close to the difference in PBLH-R and PBLH-E. The  
334 overestimation over North America at 0000 UTC, over East Asia and South Asia at  
335 1200 UTC, and over Africa at 1800 UTC can be as high as 500 m. However, PBLH  
336 over some areas, such as the Middle East at 0600 UTC and the Western United States  
337 at 1800 UTC, is slightly underestimated by around 200 m.



## 338 **6 Conclusions and summary**

339 The general underestimation of PBLH by reanalysis dataset, especially during the  
340 daytime, motivates the present analysis to generate a merged long-term high-resolution  
341 seamless continental PBLH dataset (i.e., PBLH-M) by integrating multi-modal data  
342 products, which includes 185 million high-resolution radiosondes from the years 2011  
343 to 2021, ERA5 reanalysis, and GLDAS product. The PBLH-M generated in this study  
344 has a horizontal resolution of  $0.25^{\circ} \times 0.25^{\circ}$  and a temporal resolution of 3 hours,  
345 identical to PBLH-E, but with much higher data accuracy.

346 Compared to the PBLH-R, the PBLH-M is overestimated by around  $-0.9$  m, which  
347 is considerably smaller than the bias between PBLH-R and PBLH-E (95.7 m). During  
348 the daytime, the mean and the standard derivation of bias are remarkably decreased  
349 from 300 m and 600 m (PBLH-R minus PBLH-E) to 20 m and 300 m (PBLH-R minus  
350 PBLH-M), respectively. In addition, the climatological variation of the merged PBLH  
351 dataset is highly correlated with PBLH-R, both in magnitude and spatial-temporal  
352 variation. Moreover, the climatological mean of continental PBLH-M is around 90 m  
353 higher than that of PBLH-E, which is quantitatively consistent with the comparison  
354 result of PBLH-R and PBLH-E. Overall, the merged dataset closely agrees with the  
355 radiosonde-derived PBLH in terms of magnitude and spatial-temporal variation.

356 In conclusion, the PBLH-M dataset is outstanding in terms of both spatiotemporal  
357 coverage and good accuracy. This dataset could be of importance for advancing our  
358 understanding of the PBL processes involved in air quality prediction, weather forecast,  
359 and climate projection under global warming. In the future, with more dataset available  
360 over the ocean, the global seamless PBLH dataset is warranted, and this needs more  
361 field campaigns to be deployed over the open ocean or islands in the ocean in which  
362 more intensive radiosonde balloons are launched. Besides, it is imperative to improve  
363 the observational capability of satellite-based instruments in characterizing the  
364 temperature and humidity profiles in the PBL, which no doubt helps fill the gaps of  
365 atmospheric sounding over the ocean.



366 **Author contributions**

367 JG and FH conceptualized this study. JG and JZ carried out the dataset production with  
368 comments from other co-authors. JG, JZ and JS drafted the first manuscript, and JS,  
369 KB, and RL further revised it. JS contributed to the model establish and its optimization.  
370 All authors contributed to the discussion of result interpretation and helped finalized  
371 the submission.

372

373

374 **Competing interests**

375 The contact author has declared that neither they nor their co-authors have any  
376 competing interests.

377

378 **Financial support**

379 This study is jointly supported by the Natural Science Foundation of China under grant  
380 U2142209 and 62101203, and the Fundamental Research Funds for the Central  
381 Universities, China University of Geosciences (Wuhan) (no. 162301192698), the  
382 Chinese Academy of Sciences under grant GXDA20040502, and Chinese Academy of  
383 Meteorological Sciences under grant 2021KJ029.

384 **Data availability**

385 The merged PBLH dataset and the related codes can be accessed at  
386 <https://doi.org/10.5281/zenodo.6498004> (Guo et al., 2022).

387 ERA5 data is publicly accessible at  
388 <https://cds.climate.copernicus.eu/#!/search?text=ERA5&type=dataset> (ECMWF,



389 2019). NASA GLDAS can be accessed at:  
390 [https://disc.gsfc.nasa.gov/datasets/GLDAS\\_NOAH025\\_3H\\_2.1/summary?keywords=](https://disc.gsfc.nasa.gov/datasets/GLDAS_NOAH025_3H_2.1/summary?keywords=)  
391 GLDAS (NASA, 2021).

## 392 **References**

- 393 Anderson, P. S: Measurement of Prandtl number as a function of Richardson number  
394 avoiding self-correlation, *Boundary Layer Meteorol*, 131, 345–362,  
395 <https://doi.org/10.1007/s10546-009-9376-4>, 2009.
- 396 Baklanov, A. A., Grisogono, B., Bornstein, R., Mahrt, L., Zilitinkevich, S. S., Taylor,  
397 P., Larsen, S.E., Rotach, M.W. and Fernando, H. J. S.: The nature, theory, and  
398 modeling of atmospheric planetary boundary layers, *Bull Am Meteorol*  
399 *Soc*, 92(2), 123–128, <https://doi.org/10.1175/2010BAMS2797.1>, 2011
- 400 Basha, G., and Ratnam, M. V.: Identification of atmospheric boundary layer height over  
401 a tropical station using high-resolution radiosonde refractivity profiles:  
402 Comparison with GPS radio occultation measurements, *J. Geophys. Res.*  
403 *Atmos.*, 114(D16), <https://doi.org/10.1029/2008JD011692>, 2009.
- 404 Chan, K. M., and Wood, R.: The seasonal cycle of planetary boundary layer depth  
405 determined using COSMIC radio occultation data, *J. Geophys. Res. Atmos.*,  
406 118, 12 422–12 434, <https://doi.org/10.1002/2013JD020147>, 2013.
- 407 Cooper, D. I. and Eichinger, W. E.: Structure of the atmosphere in an urban planetary  
408 boundary layer from lidar and radiosonde observations, *J. Geophys. Res.*  
409 *Atmos.*, 99(D11), 22937–22948, <https://doi.org/10.1029/94JD01944>, 1994.
- 410 Cuxart, J., and Boone A. A.: Evapotranspiration over Land from a Boundary-Layer  
411 Meteorology Perspective. *Boundary Layer Meteorol.*, 177, 427–459,  
412 <https://doi.org/10.1007/s10546-020-00550-9>, 2020.
- 413 Davis, E. V., Rajeev, K., and Mishra, M.K.: Effect of clouds on the diurnal evolution  
414 of the atmospheric boundary-layer height over a tropical coastal  
415 station, *Boundary Layer Meteorol.*, 175(1), 135–152,  
416 <https://doi.org/10.1007/s10546-019-00497-6>, 2020.



- 417 Davy, R., and Esau, I.: Differences in the efficacy of climate forcings explained by  
418 variations in atmospheric boundary layer depth, *Nat. Commun.*, 7(1), 11690.  
419 <https://doi.org/10.1038/ncomms11690>, 2016.
- 420 de Arruda Moreira, G., Guerrero-Rascado, J. L., Bravo-Aranda, J. A., Benavent-Oltra,  
421 J. A., Ortiz-Amezcuca, P., Róman, R., Bedoya-Velásquez, A. E., Landulfo, E.  
422 and Alados-Arboledas, L.: Study of the planetary boundary layer by microwave  
423 radiometer, elastic lidar and Doppler lidar estimations in Southern Iberian  
424 Peninsula, *Atmos Res.*, 213, 185–195,  
425 <https://doi.org/10.1016/j.atmosres.2018.06.007>, 2018.
- 426 Degrazia, G. A., D. Anfossi, J. C. Carvalho, C. Mangia, T. Tirabassi and Campos Velho,  
427 H. F.: Turbulence parameterisation for PBL dispersion models in all stability  
428 conditions, *Atmos. Environ.*, 34(21), 3575–3583,  
429 [https://doi.org/10.1016/S1352-2310\(00\)00116-3](https://doi.org/10.1016/S1352-2310(00)00116-3), 2000.
- 430 Ding, F., Iredell, L., Theobald, M., Wei, J., and Meyer, D.: PBL height from AIRS,  
431 GPS RO, and MERRA-2 products in NASA GES DISC and their 10-year  
432 seasonal mean intercomparison, *Earth Space Sci.*, 8,  
433 e2021EA001859, <https://doi.org/10.1029/2021EA001859>, 2021.
- 434 Dirmeyer, P. A., Wang, Z., Mbulu, M. J. and Norton, H. E.: Intensified land surface  
435 control on boundary layer growth in a changing climate, *Geophys. Res.  
436 Lett.*, 41(4), 1290–1294, <https://doi.org/10.1002/2013GL058826>, 2014.
- 437 ECMWF.: ERA5 reanalysis [data set], Retrieved from  
438 <https://cds.climate.copernicus.eu/#/search?text=ERA5&type=dataset>, 2019.
- 439 Edson, J. B., Jampana, V., Weller, R. A., Bigorre, S. P., Plueddemann, A. J., Fairall, C.  
440 W., Miller, S. D., Mahrt, L., Vickers, D., and Hersbach, H.: On the Exchange of  
441 Momentum over the Open Ocean, *J Phys Oceanogr.*, 43(8), 1589–1610,  
442 <https://doi.org/10.1175/JPO-D-12-0173.1>, 2013.
- 443 Esau, I., and Zilitinkevich, S.: On the role of the planetary boundary layer depth in the  
444 climate system. *Adv. Sci. Res.*, 4, 63, <https://doi.org/10.5194/asr-4-63-2010>,  
445 2010.



- 446 Guo, J., Li, Y., Cohen, J. B., Li, J., Chen, D., Xu, H., Liu, L., Yin, J., Hu, K., and Zhai.  
447 P.: Shift in the temporal trend of boundary layer height in China using long-  
448 term (1979–2016) radiosonde data, *Geophys. Res. Lett.*, 46, 6080–6089,  
449 <https://doi.org/10.1029/2019GL082666>, 2019.
- 450 Guo, J., Miao, Y., Zhang, Y., Liu, H., Li, Z., Zhang, W., He, J., Lou, M., Yan, Y., Bian,  
451 L., and Zhai, P.: The climatology of planetary boundary layer height in China  
452 derived from radiosonde and reanalysis data, *Atmos. Chem. Phys.*, 16, 13309–  
453 13319, <https://doi.org/10.5194/acp-16-13309-2016>, 2016.
- 454 Guo, J., Zhang, J., Yang, K., Liao, H., Zhang, S., Huang, K., Lv, Y., Shao, J., Yu, T.,  
455 Tong, B., Li, J., Su, T., Yim, S. H. L., Stoffelen, A., Zhai, P., and Xu, X.:  
456 Investigation of near-global daytime boundary layer height using high-  
457 resolution radiosondes: first results and comparison with ERA5, MERRA-2,  
458 JRA-55, and NCEP-2 reanalyses, *Atmos. Chem. Phys.*, 21, 17079–17097,  
459 <https://doi.org/10.5194/acp-21-17079-2021>, 2021.
- 460 Guo, J., Zhang, J., Shao, J.: A Harmonized Global Continental High-resolution  
461 Planetary Boundary Layer Height Dataset Covering 2017-2021 [data set],  
462 <https://zenodo.org/record/6498004>, 2022.
- 463 Hennemuth, B., and Lammert, A.: Determination of the atmospheric boundary layer  
464 height from radiosonde and lidar backscatter, *Boundary Layer Meteorol.*,  
465 120(1), 181–200, <https://doi.org/10.1007/s10546-005-9035-3>, 2006.
- 466 Hersbach, H., Bell, B., Berrisford, P., Hirahara, S., Horányi, A., Muñoz-Sabater, J.,  
467 Nicolas, J., Peubey, C., Radu, R., Schepers, D. and Simmons, A.: The ERA5  
468 global reanalysis, *Q. J. R. Meteorol. Soc.*, 146(730), 1999–2049,  
469 <https://doi.org/10.1002/qj.3803>, 2020.
- 470 Holzworth, G. C.: Estimates of mean maximum mixing depths in the contiguous United  
471 States, *Mon. Wea. Rev.*, 92, 235–242, [https://doi.org/10.1175/1520-0493\(1964\)092,0235:EOMMMD.2.3.CO;2](https://doi.org/10.1175/1520-0493(1964)092,0235:EOMMMD.2.3.CO;2), 1964.



- 473 Hu, X. M., Nielsen-Gammon, J. W. and Zhang, F.: Evaluation of three planetary  
474 boundary layer schemes in the WRF model, *J Appl Meteorol Climatol.*, 49(9),  
475 1831–1844, <https://doi.org/10.1175/2010JAMC2432.1>, 2010.
- 476 Lammert, A., and Bösenberg, J.: Determination of the con- vective boundary-layer  
477 height with laser remote sensing, *Bound.-Layer Meteor.*, 119, 159–170,  
478 <https://doi.org/10.1007/s10546-005-9020-x>, 2006.
- 479 Li, Q., Zhang, H., Cai, X. et al.: The impacts of the atmospheric boundary layer on  
480 regional haze in North China, *npj Clim Atmos Sci.*, 4(1), 1–10.  
481 <https://doi.org/10.1038/s41612-021-00165-y>, 2021.
- 482 Li, Z., Guo, J., Ding, A., Liao, H., Liu, J., Sun, Y., Wang, T., Xue, H., Zhang, H. and  
483 Zhu, B.: Aerosol and boundary-layer interactions and impact on air quality. *Natl.*  
484 *Sci. Rev.*, 4(6), 810–833, <https://doi.org/10.1093/nsr/nwx117>, 2017.
- 485 Liu, B., Y. Ma, J. Guo, W. Gong, Y. Zhang, F. Mao, J. Li, X. Guo, and Shi, Y.:  
486 Boundary layer heights as derived from ground-based radar wind profiler in  
487 Beijing, *IEEE Trans. Geosci. Remote Sens.* 57(10), 8095–8104,  
488 <https://doi.org/10.1109/TGRS.2019.2918301>, 2019.
- 489 Lou, M., J. Guo, L. Wang, H. Xu, D. Chen, Y. Miao, Y. Lv, Y. Li, X. Guo, S. Ma, and  
490 Li, J.: On the relationship between aerosol and boundary layer height in summer  
491 in China under different thermodynamic conditions. *Earth Space Sci.*, 6(5),  
492 887–901, <https://doi.org/10.1029/2019EA000620>, 2019.
- 493 McGrath-Spangler, E. L., and Denning, A. S.: Estimates of North American  
494 summertime planetary boundary layer depths derived from space-borne lidar. *J.*  
495 *Geophys. Res.*, 117, D15101, <https://doi.org/10.1029/2012JD017615>, 2012.
- 496 Min, M., Bai, C., Guo, J., Sun, F., Liu, C., Wang, F., Xu, H., Tang, S., Li, B., Di, D.  
497 and Dong, L.: Estimating summertime precipitation from Himawari-8 and  
498 global forecast system based on machine learning, *IEEE Trans Geosci Remote*  
499 *Sens.*, 57(5), 2557–2570, <https://doi.org/10.1109/TGRS.2018.2874950>, 2018.



- 500 NASA.: Global Land Data Assimilation System [data set], Retrieved from  
501 [https://disc.gsfc.nasa.gov/datasets/GLDAS\\_CLSM025\\_DA1\\_D\\_2.2/summary](https://disc.gsfc.nasa.gov/datasets/GLDAS_CLSM025_DA1_D_2.2/summary)  
502 [?keywords=GLDAS](https://disc.gsfc.nasa.gov/datasets/GLDAS_CLSM025_DA1_D_2.2/summary?keywords=GLDAS), 2021.
- 503 Petäjä, T., Järvi, L., Kerminen, VM. et al.: Enhanced air pollution via aerosol-boundary  
504 layer feedback in China, *Sci. Rep.*, 6, 18998. <https://doi.org/10.1038/srep18998>,  
505 2016.
- 506 Saha, S., Sharma, S., Kumar, K.N., Kumar, P., Lal, S. and Kamat, D.: Investigation of  
507 atmospheric boundary layer characteristics using ceilometer lidar, COSMIC  
508 GPS RO satellite, radiosonde and ERA-5 reanalysis dataset over Western Indian  
509 region, *Atmos Res.*, 268, 105999,  
510 <https://doi.org/10.1016/j.atmosres.2021.105999>, 2022.
- 511 Seibert, P., Beyrich, F., Gryning, S.-E., Joffre, S., Rasmussen, A., and Tercier,  
512 P.: Review and intercomparison of operational methods for the determination  
513 of the mixing height, *Atmos. Environ.*, 34, 1001–1027,  
514 [https://doi.org/10.1016/S1352-2310\(99\)00349-0](https://doi.org/10.1016/S1352-2310(99)00349-0), 2000.
- 515 Seidel, D. J., Ao, C. O., and Li, K.: Estimating climatological planetary boundary layer  
516 heights from radiosonde observations: Comparison of methods and uncertainty  
517 analysis, *J. Geophys. Res. Atmos.*, 115(D16),  
518 <https://doi.org/10.1029/2009JD013680>, 2010.
- 519 Seidel, D. J., Zhang, Y., Beljaars, A., Golaz, J. C., Jacobson, A.R. and Medeiros, B.:  
520 2012. Climatology of the planetary boundary layer over the continental United  
521 States and Europe, *J. Geophys. Res. Atmos.*, 117(D17),  
522 <https://doi.org/10.1029/2012JD018143>, 2012.
- 523 Stull, R. B.: *An Introduction to Boundary Layer Meteorology*. Kluwer Academic, 666  
524 pp, 1988.
- 525 Su, T., Li, Z., and Kahn, R.: Relationships between the planetary boundary layer height  
526 and surface pollutants derived from lidar observations over China: regional  
527 pattern and influencing factors, *Atmos. Chem. Phys.*, 18, 15921–15935,  
528 <https://doi.org/10.5194/acp-18-15921-2018>, 2018.



- 529 Teixeira, J., Piepmeyer, J. R., Nehrir, A. R., Ao, C. O., Chen, S. S., Clayson, C. A.,  
530 Fridlind, A. M., Lebsock, M., Mc-Carty, W., Salmun, H., Santanello, J. A.,  
531 Turner, D. D., Wang, Z., and Zeng, X.: Toward a global planetary boundary  
532 layer observing system: the NASA PBL incubation study team report, NASA  
533 PBL Incubation Study Team, 134 pp., available at:  
534 [https://science.nasa.gov/science-red/s3fs-](https://science.nasa.gov/science-red/s3fs-public/atoms/files/NASAPBLIncubationFinalReport.pdf)  
535 [public/atoms/files/NASAPBLIncubationFinalReport.pdf](https://science.nasa.gov/science-red/s3fs-public/atoms/files/NASAPBLIncubationFinalReport.pdf), last access: 28 April  
536 2022.
- 537 Wallace, J. M. and Hobbs, P. V: Atmospheric Science: An Introductory Survey,  
538 Academic Press, Burlington, MA., 2006.
- 539 Wang, X. and Wang, K.: Homogenized variability of radiosonde-derived atmospheric  
540 boundary layer height over the global land surface from 1973 to 2014, *J.*  
541 *Clim.*, 29(19), 6893–6908, <https://doi.org/10.1175/JCLI-D-15-0766.1>, 2016.
- 542 Wang, Y., A. Khalizov, M. Levy, and Zhang, R.: New Directions: Light Absorbing  
543 Aerosols and Their Atmospheric Impacts, *Atmos. Environ.*, 81, 713–715,  
544 <https://doi.org/10.1016/j.atmosenv.2013.09.034>, 2013.
- 545 Xu, Z., Chen, H., Guo, J., and Zhang, W.: Contrasting effect of soil moisture on the  
546 daytime boundary layer under different thermodynamic conditions in summer  
547 over China, *Geophys Res. Lett.*, 48, e2020GL090989. [https://doi.](https://doi.org/10.1029/2020GL090989)  
548 [org/10.1029/2020GL090989](https://doi.org/10.1029/2020GL090989), 2021.
- 549 Yang, X., Zhao, C., Guo, J., and Wang, Y.: Intensification of aerosol pollution  
550 associated with its feedback with surface solar radiation and winds in Beijing,  
551 *J. Geophys. Res. Atmos.*, 121, 4093–4099,  
552 <https://doi.org/10.1002/2015JD024645>, 2016.
- 553 Zhang, J., Guo, J. P., Zhang, S. D., and Shao, J.: Inertia-gravity wave energy and  
554 instability drive turbulence: evidence from a near-global high-resolution  
555 radiosonde dataset, *Clim. Dyn.*, 1–14, [https://doi.org/10.1007/s00382-021-](https://doi.org/10.1007/s00382-021-06075-2)  
556 [06075-2](https://doi.org/10.1007/s00382-021-06075-2), 2022.



557 Zhang, W., Guo, J., Miao, Y., Liu, H., Song, Y., Fang, Z., He, J., Lou, M., Yan, Y., Li,  
558 Y., and Zhai, P.: On the summertime planetary boundary layer with different  
559 thermodynamic stability in China: A radiosonde perspective, *J. Clim.*, 31(4),  
560 1451–1465, <https://doi.org/10.1175/JCLI-D-17-0231.1>, 2018.  
561  
562  
563  
564  
565  
566  
567  
568  
569  
570  
571  
572  
573  
574  
575  
576



577 **Table 1.** Basic information of data used in the present study, including data source, the  
578 number of stations, vertical resolution, and the years with data curation.

<b>Data source</b>	<b>Number of station</b>	<b>Vertical resolution</b>	<b>Years</b>
CMA	120	5–8 m	2011–2021
NOAA	89	5 m	2011–2021
GRUAN	8	5 m	2011–2021
CEDA	12	10 m	2011–2021
University of Wyoming	125	5–10 m	2017–2021
German Deutscher Wetterdienst	14	10 m	2011–2021

579

580

581

582

583

584

585

586

587

588

589

590



591 **Table 2.** Summary of input parameters of machine learning algorithms, and the  
 592 correlation coefficient with PBLH bias between radiosonde and ERA5 reanalysis and  
 593 its confidence level.

Parameters	Acronyms	Data sources	Correlation coefficient	Confidence level
Downward shortwave radiation	DSWR	GLDAS	0.14	100%
Downward longwave radiation	DLWR	GLDAS	0.02	100%
Latent heat flux	LHF	GLDAS	0.14	100%
Sensible heat flux	SHF	GLDAS	0.10	100%
Evapotranspiration	EP	GLDAS	0.14	100%
Transpiration	TP	GLDAS	-0.02	100%
Soil moisture 0-10cm	SM10	GLDAS	-0.04	100%
Soil moisture 10-40cm	SM40	GLDAS	-0.03	100%
Soil moisture 40-100cm	SM100	GLDAS	-0.02	100%
Soil moisture 100-200cm	SM200	GLDAS	-0.03	100%
Total precipitation rate	TPR	GLDAS	-0.02	100%
Boundary layer height	PBLH-E	ERA5	-0.10	100%
Lower tropospheric stability	LTS	ERA5	0.10	100%
Standard deviation of orography height	SDDEM	ERA5	0.06	100%
Near-surface pressure	NSP	ERA5	-0.11	100%
Near-surface temperature	NST	ERA5	0.05	100%
Near-surface wind speed	NSWS	ERA5	-0.08	100%
Local solar time	LST	-	0.17	100%

594

595



596 **Table 3.** Basic information on evaluation indices. MSE, mean squared error; RMSE,  
597 root mean square error; ABSmean, mean of the absolute bias; STD, standard derivation;  
598 RMS, root mean square.

---

---

(a) evaluation indices of the training set and test set

	MSE	RMSE	Mean	ABSmean
Train set	59176	243	-0.2	152
Predict set	136971	370	-2.8	204

---

---

(b) evaluation indices of PBLH bias

	Mean	ABSmean	STD	RMS
PBLH-R – PBLH-E	95.7	260	472	481
PBLH-R – PBLH-M	-0.9	168	241	287

---

---

599

600

601

602

603

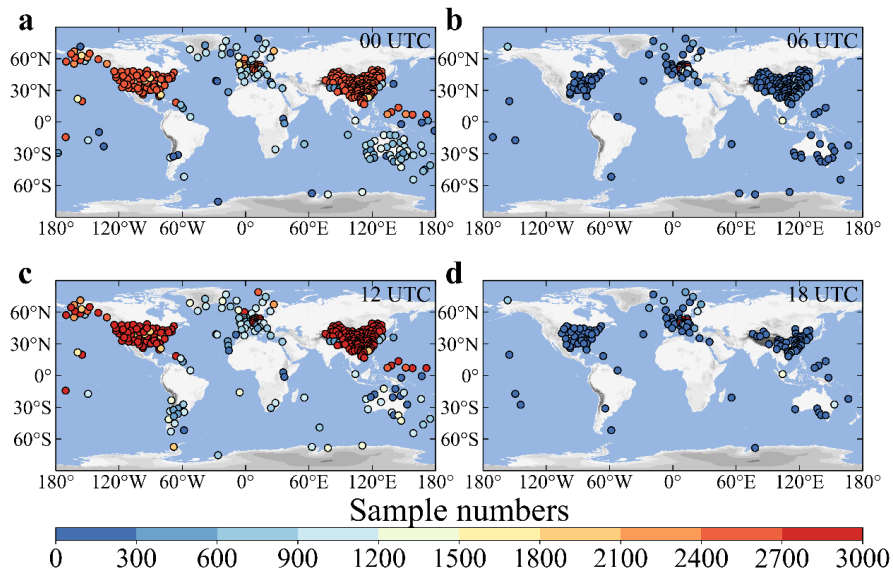
604

605

606

607

608



609

610 **Figure 1.** Spatial distribution of sample number (color circles) for each radiosonde  
611 station at 0000 (a), 0600 (b), 1200 (c), and 1800 UTC from the years 2011 to 2021.

612 Stations with less than 10 samples are not indicated.

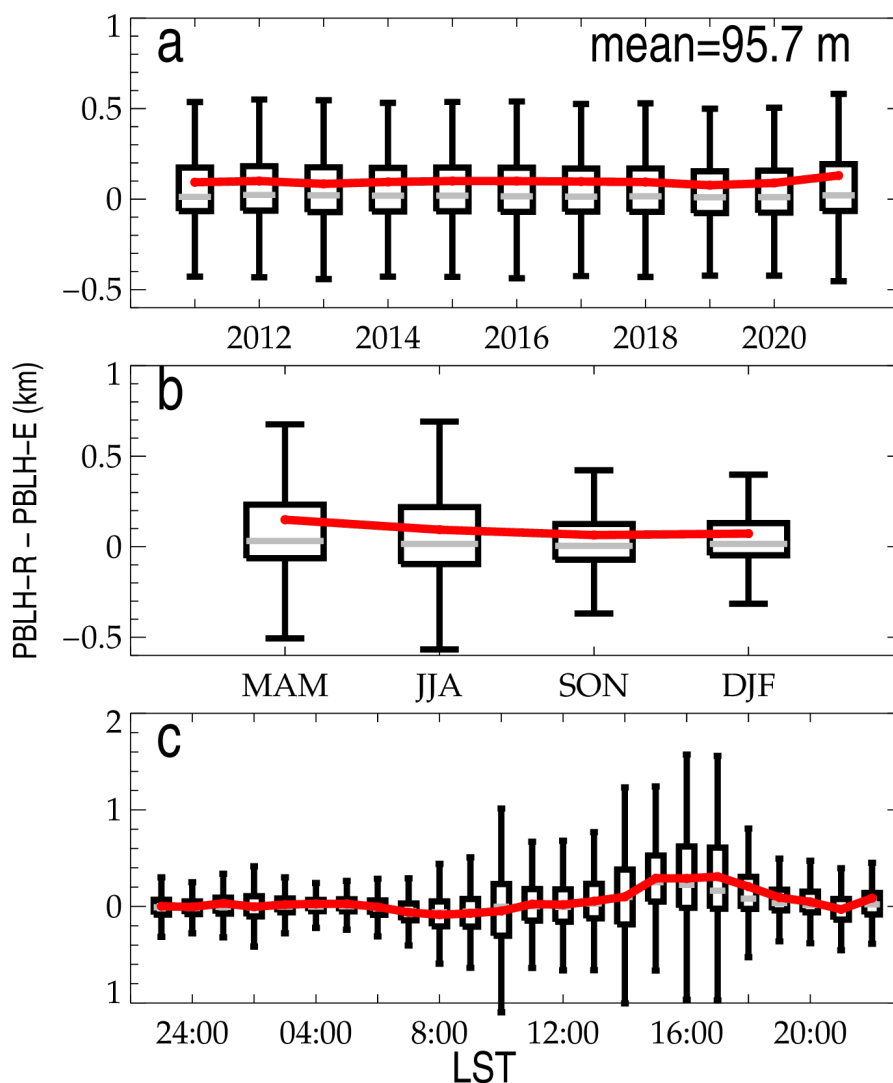
613

614

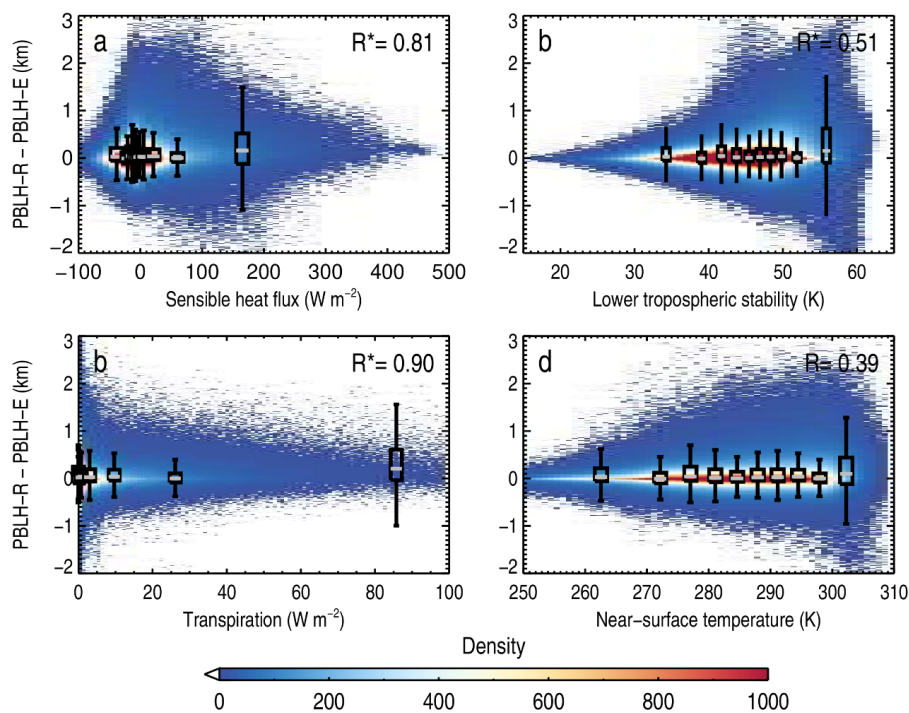
615

616

617

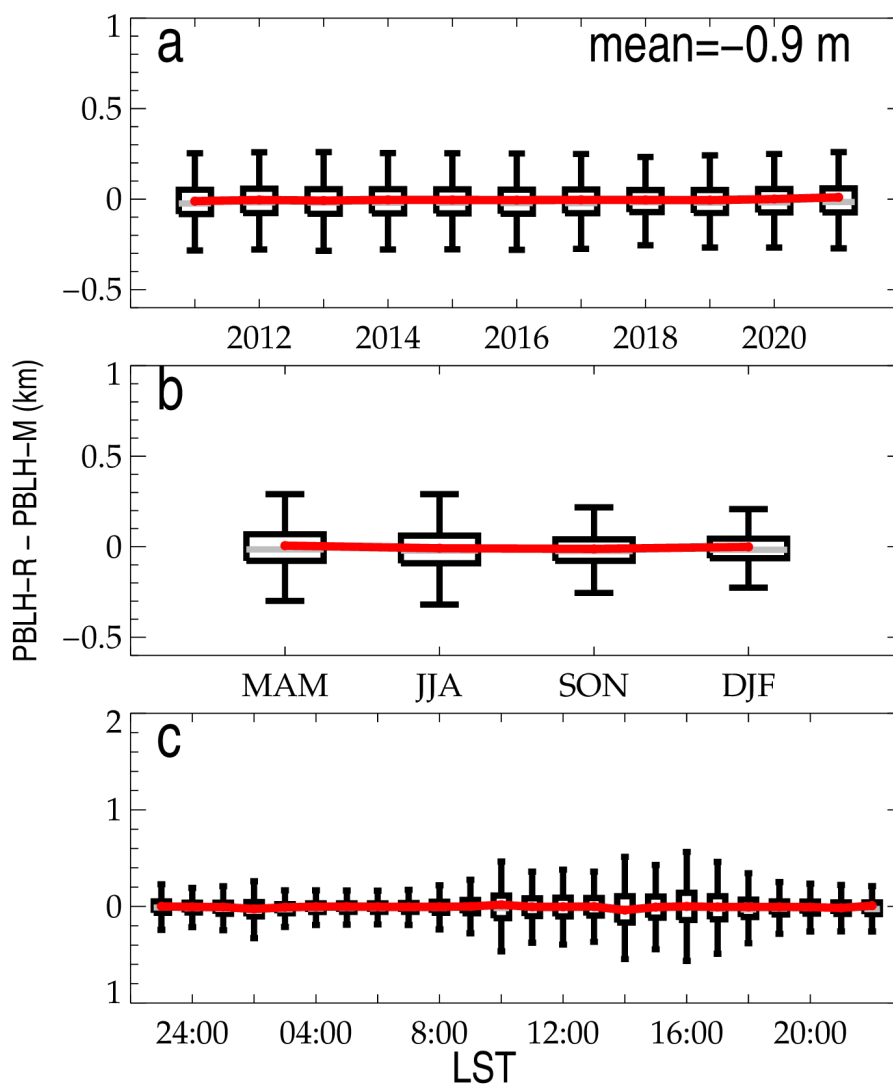


618  
619 **Figure 2.** Evolution of the difference between PBLH-E and PBLH-R at various time  
620 scales: different years (a), different seasons (b), and at different local times (c). MAM,  
621 March–April–May; JJA, June–July– August; SON, September–October–November;  
622 DJF, December–January–February. The mean bias is labelled in the upper right corner  
623 of panel (a).  
624



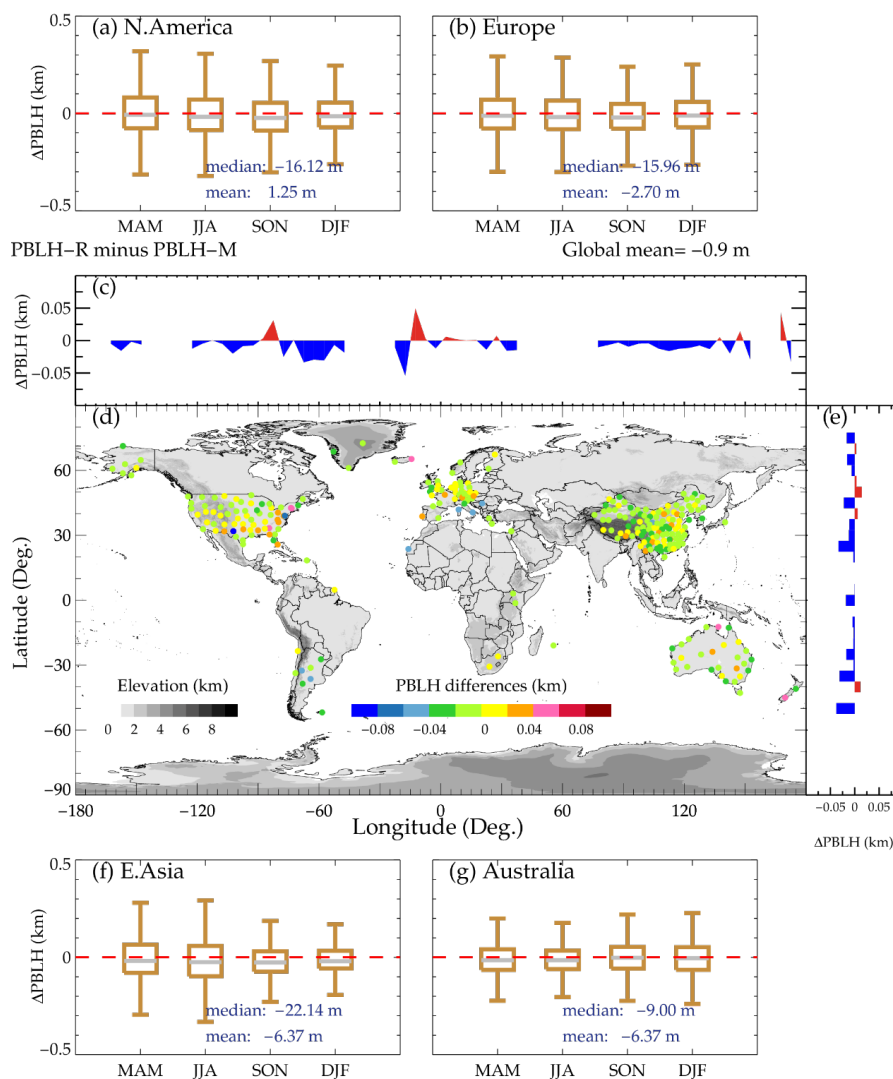
625

626 **Figure 3.** The joint distribution of the difference in PBLH-R and PBLH-E and the  
627 surface sensible heat flux (a), the lower tropospheric stability (b), transpiration (c), and  
628 the near-surface temperature (d). The box-and-whisker plots in 10 evenly intervals are  
629 overlaid in each panel, and the correlation coefficients are marked in the upper right  
630 corner of each panel, wherein the star superscripts indicate that the values are  
631 statistically significant ( $p < 0.05$ ).

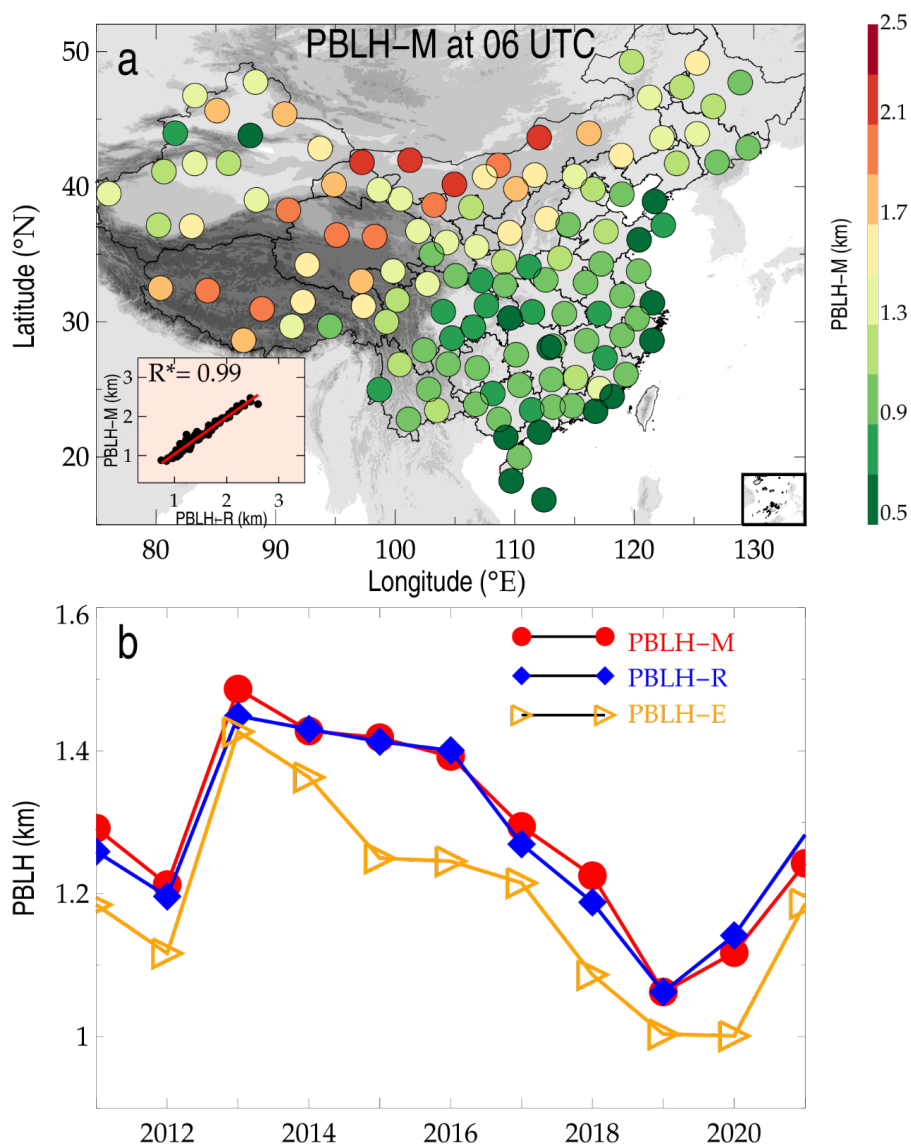


632  
633  
634  
635  
636  
637  
638  
639  
640

**Figure 4.** Similar to Figure 3, but for the difference between PBLH-R and PBLH-M.

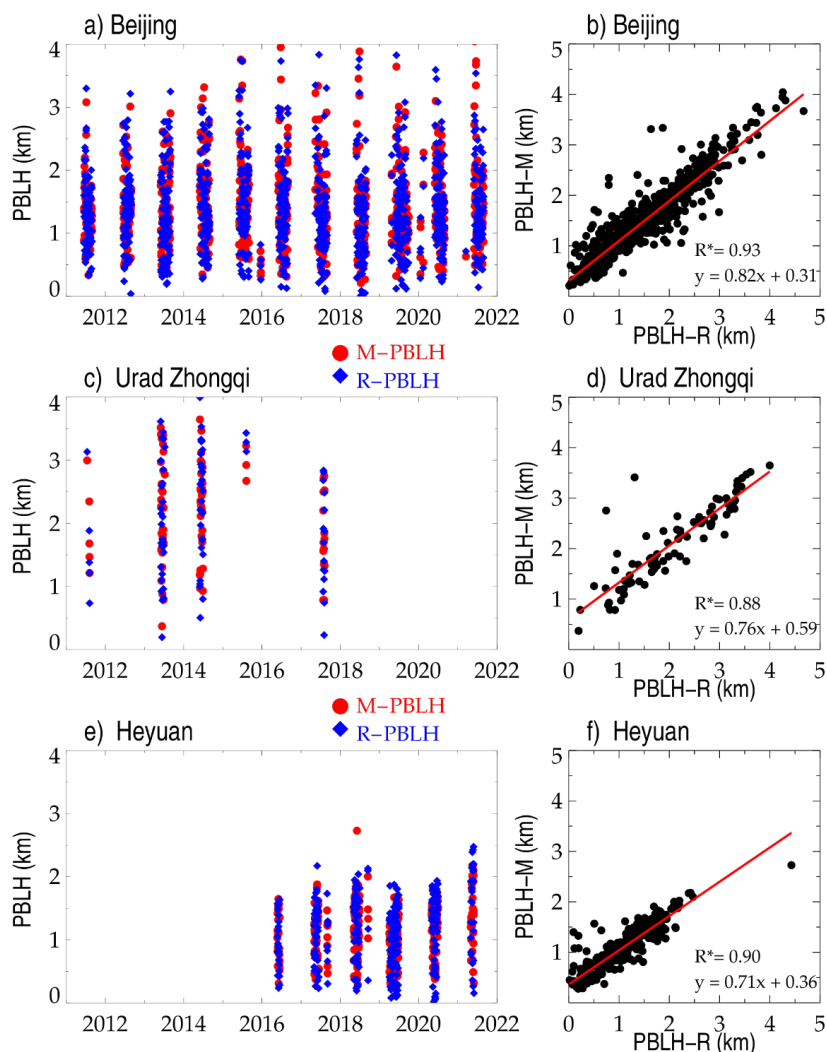


641  
 642 **Figure 5.** Spatial variations of PBLH differences between PBLH-R and PBLH-M. (d)  
 643 indicates the overall spatial distribution, and (c) and (d) illustrate its longitudinal and  
 644 latitudinal variations. (a), (b), (f), (g) represent the seasonal variations over the four  
 645 regions of interest, including North America, Europe, East Asia, and Australia. MAM,  
 646 March–April–May; JJA, June–July– August; SON, September–October–November;  
 647 DJF, December–January–February.



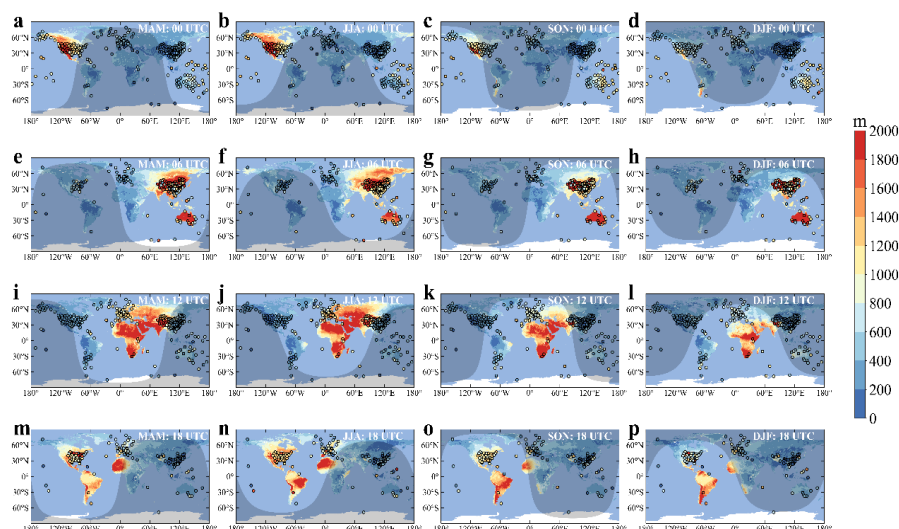
648  
649 **Figure 6.** (a) Spatial distributions of the PBLH-M at 0600 UTC across China for the  
650 years 2011 to 2021. The scatter plot in the left bottom of the panel illustrates the  
651 statistical correlation between PBLH-M and PBLH-R, where the star superscripts  
652 indicate that the values are statistically significant ( $p < 0.05$ ). Also shown are the  
653 temporal evolution of annual average PBLH-M, PBLH-R, and PBLH-E during the  
654 period 2011 to 2021 (b).

655



656  
 657 **Figure 7.** Temporal variations of PBLH-M (red) and PBLH-R (blue) at Beijing (39.8°N,  
 658 116.47°E) (a), the Urad Zhongqi station (41.3°N, 108.3°E) (b) in the Nei Monggol  
 659 Autonomous Region, and (c) the Heyuan (23.7°N, 114.7°E) station in the Guangdong  
 660 province. (b), (d), and (f) demonstrate the joint-distributions of PBLH-R and PBLH-M,  
 661 and correlation coefficients (R) and the fitted linear functions are given in the bottom  
 662 right corner, where the star superscripts indicate that the values are statistically  
 663 significant ( $p < 0.05$ ).

664  
 665

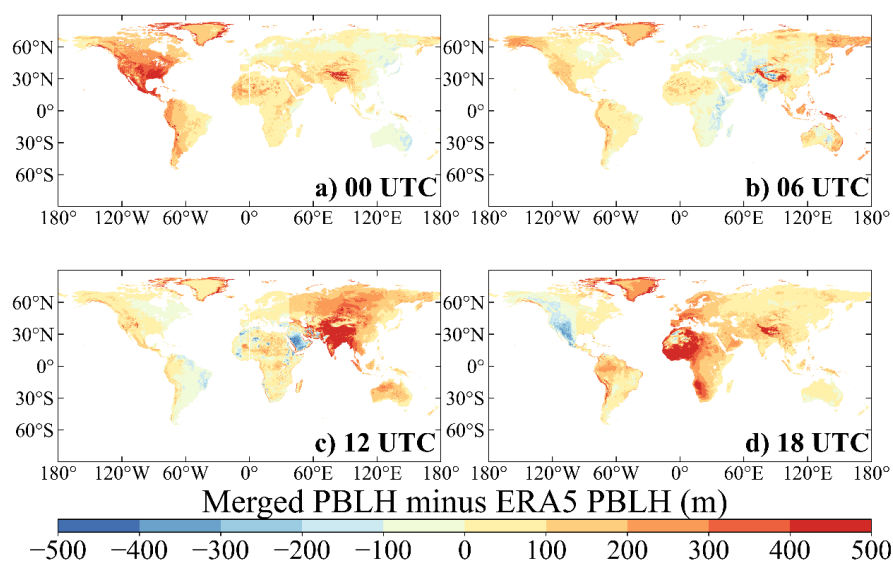


666  
667 **Figure 8.** PBLH variations produced by the merged algorithms in four seasons of 0000  
668 UTC (a-c), 0600 UTC (e-h), 1200 UTC (i-l), and 1800 UTC (m-p). The colored solid  
669 circles indicate the PBLH retrieved from high-resolution radiosondes. The shadow  
670 zones show nighttime regions, depending on the solar zenith angle on 15 April 2019  
671 (MAM), 15 July 2019 (JJA), 15 October 2019 (SON), and 15 January 2019 (DJF).  
672 MAM, March–April–May; JJA, June–July–August; SON, September–October–  
673 November; DJF, December–January–February.

674  
675  
676  
677  
678  
679  
680  
681  
682  
683  
684  
685



686



687

688 **Figure 9.** The spatial distributions of PBLH differences between the merged dataset  
689 and ERA5 reanalysis from the years 2011 to 2021 at 0000 UTC (a), 0600 UTC (b),  
690 1200 UTC (c), and 1800 UTC (d).